

Dynamics of Wrist-Worn Eccentric-Rotor Energy Harvesters

Robert Rantz^{✉*} and Shad Roundy[✉]

University of Utah, 1495 E 100 S (1550 MEK), Salt Lake City, Utah 84112, USA

 (Received 10 April 2019; revised 20 November 2019; accepted 19 May 2020; published 20 July 2020)

This work concerns the steady-state dynamics of eccentric-rotor harvesters under the excitation of a forced pendulum, selected as a simplified representation of the swinging motion of the human arm during locomotion, to better understand their use for wrist-worn energy-harvesting applications. A linearized model predicts the behavior of nonresonant eccentric-rotor devices well and provides insight into the relationship between the rotor natural frequency and transducer-imposed electrical damping. Approximate analytical solutions are obtained via perturbation methods that show that the eccentric rotor shares many characteristics of a Duffing oscillator with softening spring nonlinearity. Finally, an interesting property of the eccentric rotor's dynamics, namely, invariance of power output to changes in forcing frequency and amplitude over certain ranges of design parameters, is observed, forming the basis for a proposed resonant eccentric-rotor harvester with a wideband power output response.

DOI: [10.1103/PhysRevApplied.14.014058](https://doi.org/10.1103/PhysRevApplied.14.014058)

I. INTRODUCTION

Eccentric rotors have maintained a position of particular interest in the literature as a choice of inertial mass architecture for wrist-worn vibration energy-harvesting applications [1–7], and this harvester architecture even appears in consumer products designed to scavenge energy from the motion of the body [8,9]. These asymmetric rotational inertial vibration energy harvesters exhibit several desirable properties for a wrist-worn application, including sensitivity to both rotational and translational motion [1], a lack of hard displacement limits, and a watchlike form factor.

In spite of its popularity as an alternative to more traditional translational harvester architectures for body-worn applications, surprisingly little has been published on the complex dynamics that these devices exhibit. Although mathematical models have been proposed to describe these devices, their use has been limited primarily to the assistance of design by virtue of numerical investigation of the effects of dimensioned design parameters on power output. Much has been published on forced and parametrically excited pendula in the mathematics and dynamics literature, with Refs. [10–13] representing only a minute sample of such work, but no such publications exist that study the nonlinear model of an eccentric-rotor harvester, such as that derived in Ref. [14], for the purpose of better understanding the relationship between design parameters and power output.

Some authors have suggested [1,2,15,16] that the dynamic magnification that resonance can provide is either

infeasible or impossible to achieve for applications on the human body due to either the low-frequency high-amplitude nature of human motion, device size constraints, or both. It is perhaps due to the prevalence of this belief that nonresonant designs dominate the eccentric-rotor harvesters proposed in the literature; this work also serves as a point refutation for this assertion, as the dynamical analysis presented herein suggests that a wideband resonant eccentric-rotor harvester may indeed perform well in a wrist-worn application.

This work begins by deriving a nondimensionalized unsprung eccentric-rotor model, beginning with a dimensioned nonlinear model that has been derived and empirically validated elsewhere [14]. A dimensionless power output equation and the input excitation functions of interest are also derived. A linearized model is derived to obtain a closed-form analytical power output equation, which is useful for understanding how design parameters impact device performance; this equation is contrasted with its well-known translational energy-harvester counterpart and is followed by a brief demonstration of the linear model's validity for nonresonant eccentric-rotor harvesters. The limitations of the linear model are then examined, followed by an analysis of the nonlinear dynamics using both numerical and approximate analytical methods. The nonlinear analysis shows that the eccentric-rotor system shares many features in common with a Duffing oscillator with softening spring nonlinearity and that the primary resonance is a particularly attractive point around which to base a harvester design. The manuscript concludes with a proposal for a resonant eccentric-rotor harvester for wrist-worn application, which is compared with a nonresonant design via simulation.

*robert.rantz@utah.edu

II. SYSTEM MODEL

A planar model that governs the dynamics of an eccentric-rotor harvester has been derived and experimentally corroborated in Ref. [14] and is given by

$$\ddot{\phi} + \frac{b_e + b_m}{ml^2 + I_g} \dot{\phi} + \frac{ml}{ml^2 + I_g} a_y(t) \cos \phi - \frac{ml}{ml^2 + I_g} a_x(t) \sin \phi + \frac{k}{ml^2 + I_g} \left(\phi - \frac{\pi}{2} \right) + \ddot{\theta}(t) = 0, \quad (1)$$

where ϕ is the displacement of the eccentric rotor relative to the harvester housing coordinate frame; b_e and b_m are the electrical and mechanical linear viscous damping coefficients, respectively; m is the mass of the rotor; l is the distance from the rotating center to the rotor's center of gravity; I_g is the inertia of the rotor about its own center of gravity; k is the torsional spring stiffness; $a_y(t)$ and $a_x(t)$ are the input linear accelerations of the harvester housing (which typically include gravitational acceleration) in the y and x directions, respectively; $\ddot{\theta}(t)$ is the input angular acceleration of the housing, and overdots represent differentiation with respect to time (Fig. 1). As noted in Ref. [14], the model described by Eq. (1) may be most narrowly interpreted as a model for low-frequency electromagnetic rotational energy harvesters, although it may also be predictive for rotational energy harvesters with piezoelectric and other transducer technologies.

The parameters b_e , m , l , I_g , and k in Eq. (1) are treated as design variables, selected by the designer of the harvester. Although the designer may have some control over the degree of loss, determined by b_m , this parameter is not treated as a design variable and is instead given. Also, notably, the variables m , l , and I_g are not truly free parameters to be selected, as they are constrained by the choice

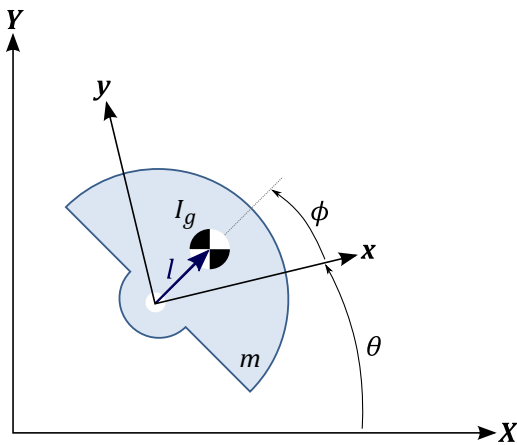


FIG. 1. Schematic of planar rotor model. Torsional spring not shown.

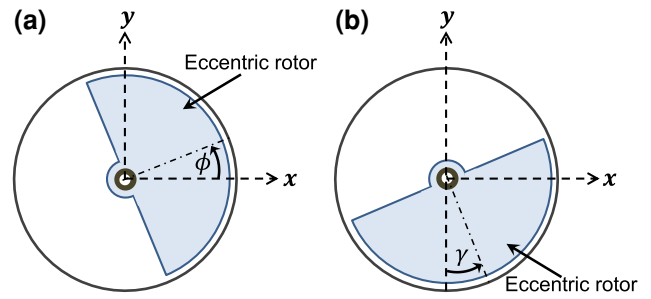


FIG. 2. Schematic of (a) the ϕ -coordinate frame used in Eqs. (1) and (2), and (b) the γ -coordinate frame used in Eq. (3).

of rotor geometry, which must be physically realizable for any practical implementation of a design.

Equation (1) is in monic form and is therefore well-defined only when the total rotational inertia about the center of rotation $ml^2 + I_g \neq 0$. Furthermore, to make Eq. (1) physically meaningful, it is assumed that b_e , b_m , m , l , I_g , and k are non-negative. As this paper is concerned with the dynamics of the eccentric-rotor harvester without a torsional spring, only the case of the unsprung rotor ($k = 0$) is considered hereafter.

By defining the effective length of the eccentric mass as $l_{\text{eff}} = (ml^2 + I_g)/(ml)$, and letting $k = 0$, Eq. (1) may be rewritten more compactly as

$$\ddot{\phi} + \frac{b_e + b_m}{ml^2 + I_g} \dot{\phi} + \frac{a_y(t)}{l_{\text{eff}}} \cos \phi - \frac{a_x(t)}{l_{\text{eff}}} \sin \phi + \ddot{\theta}(t) = 0. \quad (2)$$

To ensure that l_{eff} is well-defined, assume $m, l > 0$. Finally, Eq. (2) can be represented in an alternative coordinate frame that is the focus of the remainder of this paper (Fig. 2). Let $\gamma = \phi + \pi/2$. Equation (2) becomes

$$\ddot{\gamma} + \frac{b_e + b_m}{ml^2 + I_g} \dot{\gamma} + \frac{a_x(t)}{l_{\text{eff}}} \cos \gamma + \frac{a_y(t)}{l_{\text{eff}}} \sin \gamma + \ddot{\theta}(t) = 0. \quad (3)$$

Let $\dot{\gamma}_0(t)$ represent the time derivative of any solution to Eq. (3). The focus of this paper is Eq. (3) subject to periodic forcing and, particularly, the behavior of the time derivative of solutions after much time has passed; in other words, the steady-state behavior. With this focus in mind, it is assumed that, after a long time, $\dot{\gamma}_0(t)$ converges to a periodic solution $\dot{\gamma}(t)$; that is,

$$\lim_{\omega} \dot{\gamma}_0(t) = \dot{\gamma}(t) = \dot{\gamma}(t + T),$$

where \lim_{ω} is the ω -limit set and T is a period. Importantly, the assumption that steady state is achieved neglects the possibility of long-term aperiodic or chaotic behavior. The power output of an eccentric-rotor device modeled using

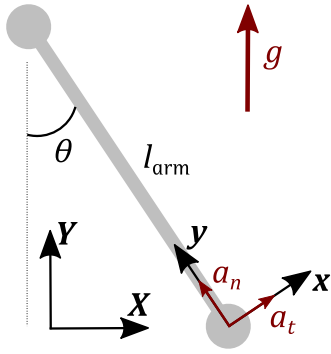


FIG. 3. Schematic of the swing arm. Coordinate frames are consistent with those of Fig. 1.

Eq. (3) is found by computing the power dissipated by the “electrical damper,” a linear viscous rotational damper with damping coefficient b_e . The average power dissipated by this damper over a period of $\dot{\gamma}$, and therefore, the steady-state power output, is

$$P = \frac{b_e}{T} \int_0^T \dot{\gamma}^2 dt. \quad (4)$$

A. Swing arm kinematics

In this study, the arm motion of humans during walking is modeled using the kinematics of a driven pendulum, with the resultant excitation at the distal end of the pendulum hereafter referred to as *swing arm* excitation (Fig. 3). Although this represents a major simplification in excitation for the purpose of analysis, actual human arm swing during locomotion shares several characteristics in common with the motion of a simple pendulum [17,18], and therefore, makes for an appropriate first-order approximation of the excitation of interest.

The tangential component of acceleration induced by the swing arm motion is given by

$$a_t = \frac{d}{dt}(l_{\text{arm}}\dot{\theta}) = l_{\text{arm}}\ddot{\theta},$$

where l_{arm} is the length of the swing arm, θ is the angular displacement of the swing arm, and overdots represent differentiation with respect to time. Similarly, the normal component of acceleration induced by the swing arm motion is given by

$$a_n = \frac{(l_{\text{arm}}\dot{\theta})^2}{l_{\text{arm}}} = l_{\text{arm}}\dot{\theta}^2.$$

Rather than consider a downward gravitational force acting on the eccentric mass directly, instead consider gravity as an effective acceleration of the housing reference frame (the \mathbf{x} - \mathbf{y} coordinate frame in Fig. 3)

The swing arm excitation is derived from the kinematics of a harmonically driven pendulum. Consider

$$\ddot{\theta}(t) = -\omega^2\theta_{\text{max}} \sin \omega t. \quad (5)$$

The total acceleration in the \mathbf{x} direction is then

$$\begin{aligned} x_{\text{total}} &= g \sin \theta + l_{\text{arm}}\ddot{\theta}, \\ &= g \sin(\theta_{\text{max}} \sin \omega t) + l_{\text{arm}}(-\omega^2\theta_{\text{max}} \sin \omega t). \end{aligned}$$

and the total acceleration in the \mathbf{y} direction is

$$\begin{aligned} y_{\text{total}} &= g \cos \theta + l_{\text{arm}}\dot{\theta}^2, \\ &= g \cos(\theta_{\text{max}} \sin \omega t) + l_{\text{arm}}(\omega\theta_{\text{max}} \cos \omega t)^2. \end{aligned}$$

It is assumed that $g, l_{\text{arm}}, \theta_{\text{max}}, \omega \geq 0$.

B. Approximation of kinematic functions

Assuming small angles for θ_{max} allows for considerable simplification of the expression for total acceleration in the \mathbf{x} direction:

$$x_{\text{total}} \approx \theta_{\text{max}}(g - l_{\text{arm}}\omega^2) \sin \omega t.$$

Similarly, the small-angle approximation can reduce the complexity of the expression for total acceleration in the \mathbf{y} direction:

$$\begin{aligned} y_{\text{total}} &\approx g \left(1 - \frac{\theta_{\text{max}}^2 \sin^2 \omega t}{2} \right) + \theta_{\text{max}}^2 l_{\text{arm}} \omega^2 \cos^2 \omega t, \\ &\approx g \left(1 - \frac{\theta_{\text{max}}^2}{4} \right) + \frac{\theta_{\text{max}}^2 l_{\text{arm}} \omega^2}{2} + \frac{\theta_{\text{max}}^2}{2} \\ &\quad \times \left(\frac{g}{2} + l_{\text{arm}} \omega^2 \right) \cos 2\omega t. \end{aligned}$$

Denoting the average over one swing arm period $2\pi/\omega$ as $\langle \cdot \rangle$, let

$$\bar{y} = g \left(1 - \frac{\theta_{\text{max}}^2}{4} \right) + \frac{\theta_{\text{max}}^2 l_{\text{arm}} \omega^2}{2} \approx \langle y_{\text{total}} \rangle.$$

Finally, let

$$\begin{aligned} x &= \theta_{\text{max}}(l_{\text{arm}}\omega^2 - g), \\ y &= \theta_{\text{max}}^2 \left(\frac{g}{2} + l_{\text{arm}}\omega^2 \right), \end{aligned}$$

where x and y (not to be confused with the \mathbf{x} - and \mathbf{y} -basis vectors for the housing coordinate frame) have dimensions of acceleration. The approximate acceleration functions $a_x(t)$ and $a_y(t)$ for swing arm excitation may now be expressed compactly as

$$a_x(t) \approx -x \sin \omega t, \quad (6)$$

$$a_y(t) \approx \bar{y} + y \cos 2\omega t. \quad (7)$$

C. Kinematic analysis

It is clear from the definition of the amplitude of the \mathbf{x} acceleration, $x = \theta_{\max}(l_{\text{arm}}\omega^2 - g)$, that the total \mathbf{x} acceleration vanishes when

$$\omega = \sqrt{\frac{g}{l_{\text{arm}}}},$$

which is the (linearized) natural frequency, sometimes referred to as the *natural pendular frequency*, of the swing arm. At slow walking speeds, fewer muscle contractions occur at the shoulder to produce additional acceleration beyond that which is due to gravity alone, which means that the arm will tend to oscillate close to its natural pendular frequency [18]; this presents a major challenge in harvesting energy at the wrist during casual locomotion, since the true \mathbf{x} accelerations at the wrist are expected to all but disappear when the arm oscillates near its natural frequency.

D. Nondimensionalization

Consider Eq. (3) subject to the swing arm excitation functions given by Eqs. (5), (6), and (7):

$$\begin{aligned} \ddot{y} + \frac{b_e + b_m}{m l^2 + I_g} \dot{y} + \omega_0^2 \left(1 + \frac{y}{\bar{y}}\right) \cos 2\omega t \sin \gamma \\ - \omega_0^2 \frac{x}{\bar{y}} \sin \omega t \cos \gamma = \omega^2 \theta_{\max} \sin \omega t. \end{aligned} \quad (8)$$

where $\omega_0 = \sqrt{\bar{y}/l_{\text{eff}}}$ is taken to be the natural frequency of the rotor. To reduce the number of parameters under consideration to only those that are essential, Eq. (8) may be nondimensionalized by introducing the following normalized variables: time $\tau = \omega_0 t$, electrical damping $\beta_e = b_e/[2\omega_0(m l^2 + I_g)]$, mechanical damping $\beta_m = b_m/[2\omega_0(m l^2 + I_g)]$, frequency ratio $\Omega = \omega/\omega_0$, \mathbf{y} acceleration amplitude $A_y = y/\bar{y}$, and \mathbf{x} acceleration amplitude $A_x = x/\bar{y}$. Equation (8) may now be written as

$$\begin{aligned} \gamma'' + 2(\beta_e + \beta_m)\gamma' + (1 + A_y \cos 2\Omega\tau) \sin \gamma \\ - A_x \sin \Omega\tau \cos \gamma = \Omega^2 \theta_{\max} \sin \Omega\tau, \end{aligned} \quad (9)$$

where the prime denotes differentiation with respect to dimensionless time τ .

It is desired to find a dimensionless analogue to the dimensioned power of Eq. (4) that can be scaled back to the dimensioned power by virtue of variables independent of dimensionless design parameters. To derive such an expression, it is useful to first define one last dimensionless parameter, $\lambda = l/l_{\text{eff}}$. Notably, given the non-negativity constraint on m , l , and I_g , and since $\lambda = m l^2/(m l^2 + I_g)$, λ is bounded from above by unity. Given that $m, l > 0$, the parameter $\lambda = 1$ only when $I_g = 0$, which corresponds to

a rotor geometry described by a point mass m at a distance l from the rotating center (i.e., the eccentric mass acts as a simple pendulum). When $0 < \lambda < 1$, the eccentric mass acts as a compound pendulum. As λ becomes small, the eccentric mass becomes less and less eccentric, losing all eccentricity when $\lambda = 0$, at which point $l = 0$ and l_{eff} is no longer well-defined. Consequentially, $\omega_0 = \sqrt{\bar{y}/l_{\text{eff}}}$ is also not well-defined, and the scale used to derive Eq. (9) breaks down. λ is, therefore, a geometric parameter describing the distribution of mass of the rotor and lies on the interval $0 < \lambda \leq 1$.

Let the dimensionless upper bound on integration be $\tau_0 = \omega_0 T$. Beginning with Eq. (4),

$$\begin{aligned} P &= \frac{b_e}{T} \int_0^T \dot{\gamma}^2 dt = \frac{2\omega_0^3(m l^2 + I_g)\beta_e}{\tau_0} \int_0^{\tau_0} \dot{\gamma}^2 d\tau \\ &= \frac{\bar{y}^2 m}{\omega} \frac{2\beta_e \Omega \lambda}{\tau_0} \int_0^{\tau_0} \dot{\gamma}^2 d\tau. \end{aligned} \quad (10)$$

Equation (10) may be divided into dimensioned and dimensionless components; analysis is greatly aided by defining a *dimensionless power* Π :

$$\Pi = \frac{2\beta_e \Omega \lambda}{\tau_0} \int_0^{\tau_0} \dot{\gamma}^2 d\tau, \quad (11)$$

such that the dimensioned power $P = \bar{y}^2 m \Pi / \omega$; stated another way, the dimensioned power P is normalized by $\bar{y}^2 m / \omega$ to give Π , as in Ref. [19].

Thus, from Eq. (11), given the input excitation parameters (A_y, A_x, θ_{\max}) and the mechanical damping β_m , the dimensionless power, $\Pi = \Pi(\beta_e, \Omega, \lambda)$, is determined over a span of dimensionless time τ_0 by the three dimensionless design parameters β_e , Ω , and λ alone. The dimensionless power is scaled to the dimensioned power P by $\bar{y}^2 m / \omega$, which is independent of the dimensionless design variables for a fixed excitation. Thus, the problem of determining the optimal m, l, I_g , and b_e given an input excitation and degree of mechanical damping reduces to determining the β_e, Ω , and λ that maximize Π , with m acting as a scaling factor for the dimensioned power output P .

E. Excitations

Several fixed excitations, treated as representative of arm swing exhibited over a range of walking speeds [18], are considered in this work (Table I). With $l_{\text{arm}} = 0.5$ m [an approximation of the mean length from the acromion (shoulder) to the ulnar styloid process (wrist) in humans [17]], the excitations are fully defined when the swing arm frequency ω and the swing arm amplitude θ_{\max} are given. The dimensionless excitation parameters A_y and A_x are computed using l_{arm} , ω , and θ_{\max} , according to their definitions given in Sec. II D.

TABLE I. List of excitations and associated parameter values used in this work.

Excitation	θ_{\max} (deg)	ω (Hz)	θ_{\max} (rad)	A_x	A_y
EX1	12.5	0.8	0.2182	0.0616	0.0418
EX2	12.5	1	0.2182	0.2131	0.0577
EX3	12.5	1.25	0.2182	0.4401	0.0816
EX4	25	0.8	0.4363	0.1168	0.1583
EX5	25	1	0.4363	0.3861	0.2090
EX6	25	1.25	0.4363	0.7474	0.2771

III. LINEARIZED SYSTEM

An analytical solution to Eq. (9) is desired to better understand the relationship between the design variables, input excitation, and power; however, due to the nonlinearity and periodic coefficients present in Eq. (9), an analytical solution is difficult, if not impossible, to obtain. Instead, linearization may provide solutions valid over a particular regime of operation. Linearization of Eq. (9) about $\gamma = 0$ yields the following linear inhomogeneous differential equation:

$$\begin{aligned} \gamma'' + 2(\beta_e + \beta_m)\gamma' + (1 + A_y \cos 2\Omega\tau)\gamma \\ = (A_x + \Omega^2\theta_{\max}) \sin \Omega\tau. \end{aligned} \quad (12)$$

Equation (12) is a forced damped Mathieu differential equation for which, once again, an analytical solution is difficult, if not impossible, to obtain. Since an analytical solution is desired, consider instead the case where A_y is negligibly small; this assumption is warranted for most of the excitations listed in Table I. Under this assumption, Eq. (12) becomes

$$\gamma'' + 2(\beta_e + \beta_m)\gamma' + \gamma = (A_x + \Omega^2\theta_{\max}) \sin \Omega\tau. \quad (13)$$

Equation (13) is a linear inhomogeneous differential equation with constant coefficients that is easily solvable. As the focus of this work is on the steady-state behavior of the eccentric rotor, only the particular solution to Eq. (13) is required for analysis. To this end, the method of undetermined coefficients is employed using the ansatz $\gamma(\tau) = A \cos \Omega\tau + B \sin \Omega\tau$ and solving for A and B . Substitution of γ' in Eq. (11) with $\tau_0 = \omega_0 T = 2\pi/\Omega$ (one swing arm cycle) gives the dimensionless power output

$$\Pi = \frac{\beta_e \Omega^2 \lambda}{\pi} \int_0^{2\pi/\Omega} \gamma'^2 d\tau = \frac{\beta_e \Omega^3 \lambda (A_x + \Omega^2 \theta_{\max})^2}{(\Omega^2 - 1)^2 + [2(\beta_e + \beta_m)\Omega]^2}. \quad (14)$$

There are several similarities and differences of note between Eq. (14) and the well-known power output equation for translational vibration energy harvesters

(TVEH) [20,21], which is provided below for the convenience of the reader:

$$P_{\text{TVEH}} = \frac{A^2 m}{\omega} \frac{\zeta_e r^3}{(r^2 - 1)^2 + [2(\zeta_e + \zeta_m)r]^2}, \quad (15)$$

where A is the input acceleration amplitude; ω is the input frequency; m is the seismic mass; ζ_e and ζ_m are the electrical and mechanical damping ratios, respectively; and r is the ratio of the input frequency to the harvester natural frequency. The leftmost fraction in Eq. (15) is similar to the dimensioned factor $\bar{y}^2 m/\omega$ used to scale Eq. (14), the eccentric-rotor dimensionless power, back to the dimensioned power. The rightmost fraction in Eq. (15) is dimensionless and very similar in form to Eq. (14) and yields several of the same results. For example, Eq. (14) exhibits a resonance peak at $\Omega \approx 1$ for systems with sufficiently low damping. Additionally, letting $\Omega = 1$ in Eq. (14) and finding the stationary point on $d\Pi/d\beta_e$ gives the optimal electrical damping ratio of $\beta_e = \beta_m$, which is similar to the results found in Refs. [19,22].

However, there are also major differences between the power output functions in the eccentric rotor and the translational case. First, there is an additional variable in the eccentric-rotor case, λ , which is required, since a particular rotor natural frequency can be achieved in an infinite number of geometric configurations for a given rotor mass m ; this is unlike the translational case, where a particular natural frequency is uniquely determined by the choice of linear spring stiffness once the seismic mass has been fixed. Because λ is entirely independent of the other dimensionless parameters on the interval $0 < \lambda \leq 1$, it is clear from the form of Eq. (14) that the optimal λ is $\lambda^* = 1$ (Fig. 4).

Second, the topology of the power function in the eccentric-rotor case and that of the translational case are different. Assuming a sufficiently low level of damping, the eccentric-rotor case described by Eq. (14) is characterized by a sharp resonance peak, but power will also grow without bound as $\beta_e, \Omega \rightarrow \infty$, unlike in the analogous

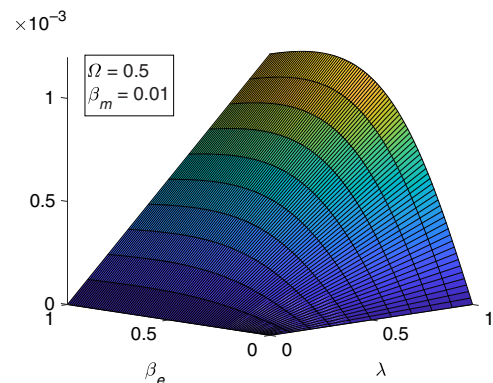


FIG. 4. Dimensionless power as a function of the geometric parameter λ and electrical damping ratio for excitation EX1.

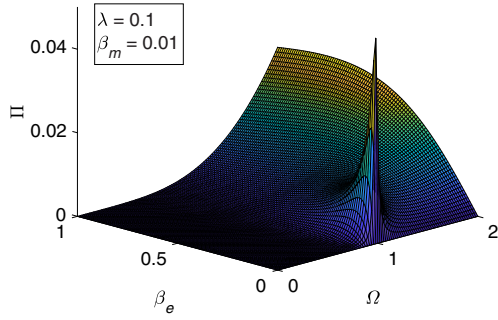


FIG. 5. Dimensionless power as a function of electrical damping ratio and frequency ratio for excitation EX1. Note the sharp resonance peak at $\Omega \approx 1$ and continued increase in dimensionless power for large β_e and Ω .

translational case; this is because a finite amount of mass may be distributed so as to produce any arbitrary amount of inertia about the center of rotation (Fig. 5). Without constraining the geometry to the practical bounds imposed by a wrist-worn energy harvester, such solutions cannot be avoided; notably, a volumetric constraint on the geometry is insufficient to preclude such solutions. All excitations in Table I produce a qualitatively similar plot for sufficiently low levels of damping.

Finally, it should be noted that the interpretation of the frequency ratio in the rotational case can be substantially different from that of the translational case. Since the input frequency ω cannot change without a corresponding change in the linear accelerations (and thus, a change in, for example, A_x), disparate values of Ω for a given excitation, such as those plotted in Fig. 5, are achieved by changing the harvester natural frequency, ω_0 , since $\Omega = \omega/\omega_0$.

Figure 5 illuminates an interesting feature of the design of eccentric-rotor harvesters: as the design moves away from $\Omega \approx 1$ (or, phrased differently, as the device becomes more *nonresonant*), the electrical damping required for optimal power output increases. Nonresonant harvesters, therefore, require a relatively high degree of electrical damping for acceptable performance.

A. A fixed geometry

The description of a rotor in terms of mass m , eccentric length l , and inertia about its own center of gravity I_g is very general; the rotor could be composed of many complex solid bodies with varying density or a collection infinitesimally small particles of mass; the rotor may even be radially symmetric under such a description, and therefore, not eccentric at all, although the use of Eq. (2) and its dimensionless counterpart Eq. (9) do prohibit this limiting case. Partially as a consequence of this generality,

the power result described by Eq. (14) is difficult to interpret with regard to practical design guidance. For example, because large Ω can result in high power output, would it be advisable to modify the geometry of a rotor to reduce the natural frequency of oscillation (increase Ω), if this comes at the cost of reducing λ ? A question such as this may be answered by constraining the geometry under consideration, which imposes relationships between the design variables in Eq. (14), such as Ω and λ .

Consider the choice of a homogeneous cylindrical sector of material density ρ with angle $\alpha = 2\psi$, radius r , and height h for the geometry of an eccentric rotor. This choice of geometry permits the expression of some design variables in Eq. (14) in terms of ψ and r :

$$m = \rho h \psi r^2, \quad \lambda = \frac{8 \sin^2 \psi}{9 \psi^2}.$$

Additionally, let the total device volume $V = \pi r^2 h$; this is the volume swept by the cylindrical sector as the rotor coordinate γ moves through all points on its configuration manifold. Using the result from linearization Eq. (14), the power per unit volume for an eccentric rotor with cylindrical sector geometry is

$$\frac{P}{V} = \frac{\bar{y}^2 m}{\omega V} \Pi = \frac{\bar{y}^2 \rho}{\omega} \frac{8 \beta_e \Omega^3 \sin^2 \psi (A_x + \Omega^2 \theta_{\max})^2}{9 \pi \psi \{(\Omega^2 - 1)^2 + [2(\beta_e + \beta_m) \Omega]^2\}}. \quad (16)$$

For a given material density ρ and input excitation, maximizing $m\lambda/V$ amounts to maximizing $\sin^2 \psi/\psi$, which occurs at a sector angle of $\alpha = 2\psi \approx 134^\circ$. A plot of power density versus frequency versus electrical damping ratio for a given excitation and mechanical damping ratio then shares the topology of Eq. (14) for a given value of λ , as in Fig. 5. Therefore, constraining the geometry of an eccentric-rotor device does not appear to obviate infinite power density solutions. If the sector angle is fixed to maximize $m\lambda/V$, then the only means by which the frequency may change for a given excitation, while preserving the volume, is by modifying the thickness of the rotor, which consequentially changes the rotor radius. To maximize power density, one then either chooses a rotor thickness and electrical damping ratio that allows for resonance with the input excitation, or one reduces the thickness indefinitely, while simultaneously increasing the electrical damping, so that power grows without bound as $\beta_e, \Omega \rightarrow \infty$; this corresponds to a device of infinitesimal thickness and infinite radius.

It is possible to express the frequency in terms of the geometric design variables as well, so that the device radius may be constrained:

$$\Omega = \omega \sqrt{\frac{3 \psi r}{4 \bar{y} \sin \psi}}.$$

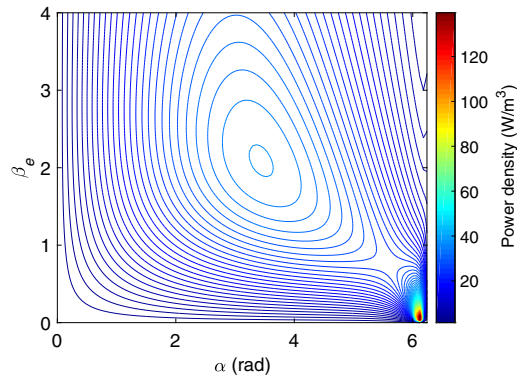


FIG. 6. Contour plot of power density versus rotor sector angle and electrical damping ratio under a particular swing arm excitation.

Substitution of this result into Eq. (16) yields a very complex expression for power density that warrants a brief numerical investigation. Consider a tungsten ($\rho = 19000 \text{ kg m}^{-3}$) cylindrical sector eccentric-rotor device with a volume of $V = 1 \text{ cm}^3$ and thickness 2 mm, requiring a radius $r \approx 12.6 \text{ mm}$. Using a swing arm excitation described by a swing arm length of $l_{\text{arm}} = 0.5 \text{ m}$, swing frequency of $\omega = 0.91 \text{ Hz}$, and a swing amplitude of $\theta_{\text{max}} = 18^\circ$, with a device mechanical damping ratio of $\beta_m = 0.0024$, a plot of power versus sector angle versus damping ratio may be generated (Fig. 6).

The power density surface presented in Fig. 6 now only contains two peaks. The first larger peak corresponds to resonance with the swing arm excitation. To achieve resonance, the rotor requires a very large sector angle. The second peak occurs at a sector angle of $\alpha \approx 3.44 \text{ rad} \approx 197^\circ$ and electrical damping ratio $\beta_e \approx 2.08$. This corresponds to a nonresonant design, and the maximizer agrees with optimization results for the nonlinear system of Eq. (1) presented in Ref. [14] very closely.

IV. NONLINEAR DYNAMICAL ANALYSIS

To observe the correspondence between the power output of the nonlinear system and its linearization, consider a plot of dimensionless power Π vs Ω for a fixed amount of damping ($\beta_e = 0.02$, $\beta_m = 0$) and fixed $\lambda = 1$, in which the linearized system power output Ref. (14) is evaluated, and the nonlinear system of Eq. (9) is numerically solved for use in Eq. (11) over a range of Ω values. The result, using EX1 as the input excitation, is shown in Fig. 7.

In spite of the mild excitation, it is clear from Fig. 7 that the linearization fails to predict the sharp onset of the primary resonance peak for the nonlinear system at $\Omega \approx 0.8$, and consequently overpredicts the power output at the linear resonance of $\Omega \approx 1$. The linearization does not capture the leftward bending of the nonlinear primary resonance at all. However, it appears that the linearized result agrees

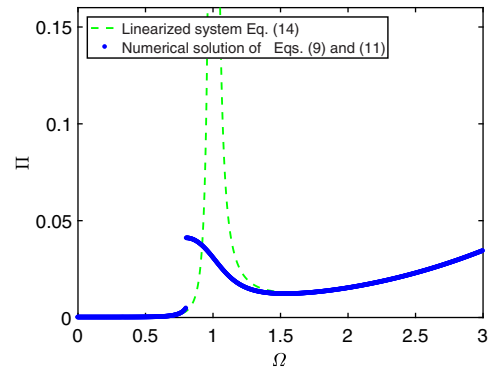


FIG. 7. Numerical versus analytical (linearization) results for power versus frequency ratio using EX1 input.

closely with the nonlinear system, as long as Ω is far from the primary resonance peak. Consider a similar plot to that of Fig. 7, but using the much more vigorous EX5 as the excitation input, shown in Fig. 8.

As seen in Fig. 8, the predictive power of the linearization is much worse for the higher-energy EX5 excitation, which is to be expected due to the small angle approximation used to derive Eq. (14), and additional nonlinear behavior is evident. A very wide high-power peak now appears near $\Omega \approx 2.5$; several scattered higher-power points also lie above this peak, which are not shown in Fig. 8 to improve the scale of the plot. Additionally, a sharp peak now clearly appears at $\Omega \approx 1/3$, although it should be noted that this peak is present for all excitations in Table I, albeit at much smaller magnitudes under light excitation, which is why this peak cannot be seen with the scale used in Fig. 7. These additional peaks are referred to as *secondary resonances*. Additional nonlinear behavior can also be observed in Fig. 8 (for example, near $\Omega \approx 1.5$), but are much less consistent between excitations.

To develop a theory to explain the nonlinear behavior exhibited by the eccentric-rotor system, approximate

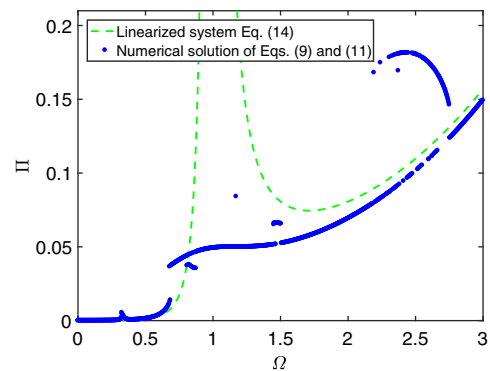


FIG. 8. Numerical versus analytical (linearization) results for power versus frequency ratio using EX5 input.

solutions are sought using perturbation methods. All simulations carried out for the remainder of this section assume $\beta_e = 0.02$, $\beta_m = 0$, and $\lambda = 1$.

A. System approximation

Consider the following approximation to Eq. (9):

$$\gamma'' + 2(\beta_e + \beta_m)\gamma' + (1 + A_y \cos 2\Omega\tau) \left(\gamma - \frac{1}{6}\gamma^3 \right) - A_x \sin \Omega\tau \left(1 - \frac{1}{2}\gamma^2 \right) = \Omega^2 \theta_{\max} \sin \Omega\tau. \quad (17)$$

Equation (17) is derived by taking the Taylor series of the trigonometric functions in Eq. (9) about $\gamma = 0$ (the Maclaurin series) and retaining the first two nonzero terms in the series.

The approximate system of Eq. (17) will be used to study Eq. (9) by employing perturbation methods. Equation (17) may be rewritten as

$$\gamma'' + \gamma + \epsilon \left[2(\bar{\beta}_e + \bar{\beta}_m)\gamma' + \bar{A}_y \cos 2\Omega\tau \gamma + \frac{1}{2}\bar{A}_x \sin \Omega\tau \gamma^2 - \gamma^3 \right] + O(\epsilon^2) = F \sin \Omega\tau, \quad (18)$$

where ϵ is a small, but finite, dimensionless quantity that indicates the degree of the perturbation, the substitutions $\beta_e = \epsilon\bar{\beta}_e$, $\beta_m = \epsilon\bar{\beta}_m$, $A_y = \epsilon\bar{A}_y$, and $A_x = \epsilon\bar{A}_x$ are used to track parameters that are considered small and $F = A_x + \Omega^2\theta_{\max}$. Given that the term $O(\epsilon^2) = -\epsilon^2\bar{A}_y \cos 2\Omega\tau \gamma^3$, it is clear that Eq. (17) is recovered from Eq. (18) when $\epsilon = 1/6$, which is considered small enough for satisfactory results, similar to Ref. [[23], pp. 133–134].

One may be concerned that the forcing amplitude F , which is not treated as small, contains A_x , which is treated as small. However, consider the excitations of Table I; for some of the excitations, such as EX1, A_x is certainly small. For other excitations, such as EX3, EX5, or EX6, A_x is arguably a large term; for this reason, it may perhaps best be considered a *borderline case*. On the other hand, $A_x/2$, which appears in a different role in a parametric forcing term in Eq. (17), is a much clearer case of a small term. Additionally, when Ω is small, the $\Omega^2\theta_{\max}$ term in F is very small, which means A_x will dominate the forcing amplitude; if this is ignored, the accuracy of the unperturbed solution will suffer greatly, since it is already clear that Eq. (13) accurately captures much of the dynamics for small Ω . For this reason, the somewhat unorthodox assumption that A_x is large, but $A_x/2$ is not, is used in the analysis whenever strong forcing is considered.

A uniform approximate solution to Eq. (18) is sought in the form

$$\gamma(\tau, \epsilon) = \gamma_0(T_0, T_1, T_2, \dots) + \epsilon\gamma_1(T_0, T_1, T_2, \dots) + \dots, \quad (19)$$

where one writes $\gamma = \gamma(\tau; \epsilon)$, with the parameter ϵ separated by a semicolon, since γ is a function of both the independent variable τ and parameter ϵ . When $\epsilon = 0$, Eq. (18) becomes linear and its solution is denoted γ_0 . Terms in the series in Eq. (19) of $O(\epsilon)$ and higher are corrections to the terms that come before, called the *correction series*, with the goal of additional terms yielding an asymptotic approximation to the solution of Eq. (18). When one retains a single term in the correction series — that is, terms up to $O(\epsilon)$ — then Eq. (19) is called a *first-order expansion*. Because functional dependence of γ on τ and ϵ is not disjoint, the solution approximation is dependent on the combination of $\epsilon\tau$ terms, as well as on individual τ and ϵ , the solution may be written as $\gamma(\tau; \epsilon) = \hat{\gamma}(\tau, \epsilon\tau, \epsilon^2\tau, \dots; \epsilon) = \hat{\gamma}(T_0, T_1, T_2, \dots; \epsilon)$, with $T_0 = \tau$, $T_1 = \epsilon\tau$, $T_2 = \epsilon^2\tau$, etc., representing different timescales, since ϵ is a small parameter. First-order expansions are the focus of this section, and such expansions may be obtained without actually having to solve for γ_1 ; only secular terms in the expression for γ_1 need be considered, which determine the dependence of γ_0 on T_1 [[24], pp. 122–126]. Thus, solutions in this section are in the form

$$\gamma(\tau; \epsilon) = \gamma_0(T_0, T_1) + \epsilon\gamma_1(T_0, T_1) + \dots, \quad (20)$$

where only the γ_0 term, herein denoted simply as γ , needs to be found, and $O(\epsilon)$ terms are neglected. The methods of variation of parameters and averaging are used to approximate solutions to Eq. (17).

A final remark before the analysis: applying the method of averaging to systems with both quadratic and cubic nonlinearities can sometimes give erroneous results due to interactions between approximation orders; such an interaction is shown to occur between first- and second-order approximations when a third-order approximation is sought for a system with quadratic and cubic nonlinearities in Ref. [[24], pp. 168–169]. Although Eq. (18) differs significantly from this example, and only a first-order approximation is desired, the analysis is nevertheless validated by comparing predictions made by the perturbation solutions of Eq. (18) to those made using numerical integration of Eq. (9).

B. Secondary resonances

To apply the method of averaging to the secondary resonances, the method of variation of parameters is first applied. The solution of Eq. (18) with $\epsilon = 0$ is

$$\gamma = a \cos(\tau + b) + 2\Lambda \sin \Omega\tau, \quad (21)$$

where the *free-oscillation* term is $a \cos(\tau + b)$ with a and b as variables, which are sometimes referred to as *parameters*, and $\Lambda = (A_x + \Omega^2\theta_{\max})/[2(1 - \Omega^2)]$. Notably, Eq. (21) contains a term with a small divisor, Λ , that becomes large as $\Omega \rightarrow 1$; the existence of this term

is why the primary and secondary resonances are treated separately in this analysis.

Substitution of Eq. (21) into Eq. (18), with subsequent simplification, reveals that the dynamics of the parameters of Eq. (21) are governed by

$$\begin{aligned} \frac{\partial a}{\partial T_1} &= -(\bar{\beta}_e + \bar{\beta}_m)a + \left(\frac{\bar{A}_x a^2}{16} - \frac{3\Lambda a^2}{4} \right) \cos[(3 - \Omega)\tau + 3b] + \left(\Lambda^3 - \frac{\bar{A}_x \Lambda^2}{4} + \frac{\bar{A}_y \Lambda}{2} \right) \cos[(1 - 3\Omega)\tau + b] + \text{OT}, \\ a \frac{\partial b}{\partial T_1} &= -3\Lambda^2 a + \frac{\bar{A}_x \Lambda a}{2} - \frac{3a^3}{8} + \left(-\frac{\bar{A}_x a^2}{16} + \frac{3\Lambda a^2}{4} \right) \sin[(3 - \Omega)\tau + 3b] \\ &\quad + \left(-\Lambda^3 + \frac{\bar{A}_x \Lambda^2}{4} - \frac{\bar{A}_y \Lambda}{2} \right) \sin[(1 - 3\Omega)\tau + b] + \left(3\Lambda^2 a - \frac{\bar{A}_x \Lambda a}{2} + \frac{\bar{A}_y a}{2} \right) \cos 2\Omega\tau + \text{OT}, \end{aligned} \quad (22)$$

where the substitution $\partial/\partial T_0 = \epsilon \partial/\partial T_1$ allows for elimination of ϵ and OT refers to other terms that are immaterial with regard to the method of averaging near the secondary resonances, such as $\sin[(1 + 3\Omega)\tau + b]$ or $\cos[(3 + \Omega)\tau + b]$, as these rapidly varying terms average to zero for the secondary resonances near $\Omega \approx 3$ and $\Omega \approx 1/3$. The terms in Eq. (22) are examined to demarcate frequencies of interest for the analysis.

1. Case 1: $\Omega \approx 3$

Consideration of the slowly varying terms in Eq. (22), equivalent to vector field averaging, allows for the derivation of the frequency response relating the amplitude of the free-oscillation term to the frequency $\sigma = (\Omega - 3)/\epsilon$,

$$\begin{aligned} 81a^4 + 64 \left[\frac{81\Lambda^2}{4} - \frac{27\bar{A}_x \Lambda}{8} + \frac{9\sigma}{4} - \frac{5}{2}(\bar{A}_x - 12\Lambda)^2 \right] a^2 \\ + 16(18\Lambda^2 - 3\bar{A}_x \Lambda + 2\sigma)^2 + 64(\bar{\beta}_e + \bar{\beta}_m)^2 = 0, \end{aligned} \quad (23)$$

which is quadratic in a^2 and easily solved. For solutions satisfying $a^2 \in \mathbb{R}$, the discriminant of the solution satisfying Eq. (23) must be positive.

Equation (23) was derived by neglecting the $a = 0$ solution, which is a solution of particular interest, since this implies that the free-oscillation term in Eq. (21) vanishes. The stability of this solution is discussed in Sec. IV D.

The solution for the case of $\Omega \approx 3$ is given by

$$\gamma = a \cos\left(\frac{1}{3}\Omega\tau - \frac{1}{3}d\right) + 2\Lambda \sin \Omega\tau + O(\epsilon), \quad (24)$$

up to $O(\epsilon)$ with (dimensionless) time derivative

$$\gamma' = -\frac{1}{3}a\Omega \sin\left(\frac{1}{3}\Omega\tau - \frac{1}{3}d\right) + 2\Lambda\Omega \cos \Omega\tau + O(\epsilon), \quad (25)$$

where $d = T_1\sigma - 3b$. Notably, the frequency of the free-oscillation term is $\Omega/3$, or one-third of the dimensionless frequency ratio; consequentially, such secondary resonances are known as *subharmonic resonances of order one-third* [[24], pp. 197–198]. Such resonances can exhibit a very large response, in spite of being far from $\Omega \approx 1$.

2. Case 2: $\Omega \approx 1/3$

Consideration of the slowly varying terms in Eq. (22) allows for the derivation of the frequency response relating the amplitude of the free-oscillation term to the frequency $\sigma = (3\Omega - 1)/\epsilon$,

$$\begin{aligned} \frac{9}{64}a^6 + \left(\frac{9\Lambda^2}{4} - \frac{3\bar{A}_x \Lambda}{8} + \frac{3\sigma}{4} \right) a^4 \\ + \left[\left(3\Lambda^2 - \frac{\bar{A}_x \Lambda}{2} + \sigma \right)^2 + (\bar{\beta}_e + \bar{\beta}_m)^2 \right] a^2 \\ - 2 \left(\Lambda^3 - \frac{\bar{A}_x \Lambda^2}{4} + \frac{\bar{A}_y \Lambda}{2} \right)^2 = 0, \end{aligned} \quad (26)$$

which is a cubic equation in a^2 . The roots of Eq. (26) satisfying $a^2 \in \mathbb{R}$ give the steady-state amplitude of the free-oscillation for a given σ .

The solution for the case of $\Omega \approx 1/3$ is given by

$$\gamma = a \cos(3\Omega\tau - d) + 2\Lambda \sin \Omega\tau + O(\epsilon), \quad (27)$$

up to $O(\epsilon)$ with time derivative

$$\gamma' = -3a\Omega \sin(3\Omega\tau - d) + 2\Lambda\Omega \cos \Omega\tau + O(\epsilon). \quad (28)$$

Notably, the frequency of the free-oscillation term is 3Ω , or 3 times the dimensionless frequency ratio; consequentially, such secondary resonances are known as *superharmonic resonances of order three* [[24], p. 202].

3. Case 3: $\Omega \approx 0$

Since τ appears explicitly in the governing equation, it is unclear which timescale (T_0 or T_1) is appropriate to describe a term such as $\cos 2\Omega\tau$. If $\Omega \approx 0$, then $\cos 2\Omega\tau$ is slowly varying. Let $\Omega = \epsilon\sigma$ to express the smallness of Ω and write $\cos 2\Omega\tau = \cos 2\sigma\epsilon\tau = \cos 2\sigma T_1$. There are no slowly varying terms in the a differential equation, but there is $\cos 2\Omega\tau$ in the b differential equation, which is slowly varying at $\Omega \approx 0$. The parameters are thus governed by

$$\begin{aligned} \frac{\partial a}{\partial T_1} &= -(\bar{\beta}_e + \bar{\beta}_m)a, \\ a \frac{\partial b}{\partial T_1} &= \left(3\Lambda^2 a - \frac{\bar{A}_x \Lambda a}{2} + \frac{\bar{A}_y a}{2} \right) \cos 2\sigma T_1. \end{aligned} \quad (29)$$

From Eq. (29), it is clear that

$$a = a_0^{-\left(\bar{\beta}_e + \bar{\beta}_m\right)T_1},$$

which indicates that the free-oscillation term in Eq. (21) vanishes at steady state, leaving only the $2\Lambda \sin \Omega\tau$ term; this is the linearized solution presented in Sec. III, albeit without damping.

4. Case 4: Ω away from 0, 1, 3, and 1/3

In this case, the only slowly varying terms in Eq. (22) are the constant terms. Thus, the parameters are governed by

$$\begin{aligned} \frac{\partial a}{\partial T_1} &= -(\bar{\beta}_e + \bar{\beta}_m)a, \\ a \frac{\partial b}{\partial T_1} &= -3\Lambda^2 a + \frac{\bar{A}_x \Lambda a}{2} - \frac{3a^3}{8}. \end{aligned}$$

Hence, both parameters rapidly approach zero, as in the $\Omega \approx 0$ case, and Eq. (21) becomes the solution to an undamped harmonically excited linear oscillator at steady state. This explains why the solution to the linearized system Eq. (13) presented in Sec. III, which also includes the additional effect of damping, is predictive of the dynamics of Eq. (9) far from any resonance peaks.

C. Primary resonance

Due to the small divisor term in Eq. (21), an alternative to Eq. (18) is proposed as the perturbed system for analysis:

$$\begin{aligned} \gamma'' + \gamma + \epsilon \left[2(\bar{\beta}_e + \bar{\beta}_m)\gamma' + \bar{A}_y \cos 2\Omega\tau \gamma + \frac{1}{2}\bar{A}_x \sin \Omega\tau \gamma^2 \right. \\ \left. - \gamma^3 - (\Omega^2 \bar{\theta}_{\max} + \bar{A}_x) \sin \Omega\tau \right] + O(\epsilon^2) = 0, \end{aligned} \quad (30)$$

where the substitution $\bar{\theta}_{\max} = \epsilon\theta_{\max}$ is introduced to reflect the smallness of the forcing term, which is valid for weak excitation. The analysis then proceeds the same as that with the secondary resonances. The solution of Eq. (30) with $\epsilon = 0$ is

$$\gamma = a \cos(\tau + b), \quad (31)$$

where a and b again act as solution parameters with dynamics to be determined. Notice that Eq. (31) no longer contains the small divisor term. Substitution of Eq. (31) into Eq. (30), with subsequent simplification, reveals that the dynamics of the parameters of Eq. (31) are governed by

$$\begin{aligned} \frac{\partial a}{\partial T_1} &= -(\bar{\beta}_e + \bar{\beta}_m)a + \left(\frac{\bar{A}_x a^2}{16} - \frac{\Omega^2 \bar{\theta}_{\max}}{2} - \frac{\bar{A}_x}{2} \right) \cos d \\ &\quad - \frac{\bar{A}_y a}{4} \sin 2d, \\ a \frac{\partial d}{\partial T_1} &= a\sigma + \frac{3a^3}{8} + \left(-\frac{3\bar{A}_x a^2}{16} + \frac{\Omega^2 \bar{\theta}_{\max}}{2} + \frac{\bar{A}_x}{2} \right) \sin d \\ &\quad - \frac{\bar{A}_y a}{4} \cos 2d. \end{aligned} \quad (32)$$

The form of Eq. (32) differs from the vector fields that govern the parameters of the secondary resonance solutions, as well as from the system of differential equations that describes the parameters for a first-order approximation of the weakly forced Duffing oscillator [[24], pp. 205–208], in two important ways. First, the amplitudes of the $\cos d$ and $\sin d$ terms are not simply the inverse of each other; this appears to be a consequence of the $\sin \Omega\tau$ parametric excitation term in Eq. (30). Second, there are $\sin 2d$ and $\cos 2d$ terms in Eq. (32); this appears to be a consequence of the $\cos 2\Omega\tau$ parametric excitation term in Eq. (30). Due to the additional complexity, even solving for the fixed points of Eq. (32) represents a challenge. However, some information may be ascertained by examination. The steady-state values of a are given by $\partial a / \partial T_1 = 0$, yielding a quadratic in a . Similarly, letting $a \partial d / \partial T_1 = 0$ gives a cubic equation in a . Treating Eq. (32) as a system of polynomials in a with a finite number of solutions,

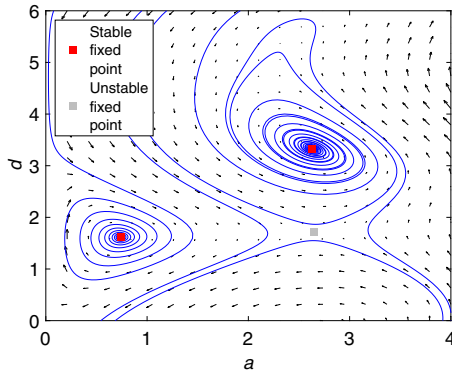


FIG. 9. Phase portrait of the a - d plane for Eq. (32), which governs the primary resonance, under EX5 at $\Omega = 0.6$. Two stable spirals represent attractors for higher and lower amplitude solution branches, and a separatrix is formed by the unstable saddle point.

then, by Bézout's theorem, there are at most six solutions, counting multiplicity. Equation (32) is also invariant under the transformation $d \rightarrow d \pm n2\pi$, $n \in \mathbb{Z}$. Thus, the steady-state solution amplitude may attain up to six values, and the interval of interest for d may be restricted to $d \in [0, 2\pi)$. For a visualization of the phase plane, see Fig. 9.

Since $b = \sigma T_1 - d$, $\Omega = 1 - \epsilon\sigma$, and $T_1 = \epsilon\tau$, the solution for the case of $\Omega \approx 1$ is given by

$$\gamma = a \cos(\Omega\tau - d) + O(\epsilon), \quad (33)$$

up to $O(\epsilon)$ with (dimensionless) time derivative

$$\gamma' = -a\Omega \sin(\Omega\tau - d) + O(\epsilon). \quad (34)$$

D. Validation of analysis

The results presented in this section are derived from Eqs. (17) and (30) — approximations of the original system of interest, Eq. (9) — using approximate analytical methods. To assess the validity of the perturbation solutions (and the system approximations from which they are derived) in predicting the behavior of the original system, a brief comparison between numerical solutions of Eq. (9)

and the perturbation solutions of Eqs. (24), (27), and (33) is presented in this section.

The perturbation solutions are validated in two ways. First, since the amplitude of the free-oscillation terms is the direct output of the averaging method, it is appropriate to compare the amplitude of numerical solutions of Eq. (9) to the amplitude of the analytical approximations of Eqs. (24), (27), and (33). Since the solutions are not typically simple sinusoids, the amplitude is approximated in all cases by computing half of the difference between the maximum and minimum values attained by the solutions at steady state. Comparisons of power output are used as the second method for validating the analysis, which is accomplished by the use of the second component (velocity) of the numerical solution to Eq. (9) and the perturbation solution derivatives of Eqs. (25), (28), and (34), in Eq. (11) during steady state.

The numerical simulations are performed over a length of 200 swing arm cycles of period $2\pi/\Omega$. Amplitude and power values are computed over some final number of swing arm cycles to be determined, as the solutions near the end of the simulation timespan are presumed to represent a steady-state condition. The (smallest) period of Eq. (27) is $6\pi/\Omega$, or three swing arm cycles; this represents the perturbation solution with the longest period, and therefore, three swing arm cycles represents a fair choice for the final number of cycles over which output is computed. However, to account for the possibility of a subharmonic at $\Omega \approx 2$, or any other unexpected nonlinear behavior, the final 30 swing arm cycles of the simulation are instead selected to be representative of a steady-state condition. Figures 7 and 8 are generated under this assumption.

Due to the complexity of the equations, a numerical approach is taken to find the fixed points of Eq. (32), the primary resonance. For each value of Ω to be plotted, a grid of 1024 initial guess points is formed in the region $-5 \leq a \leq 5$, $0 < d \leq 2\pi$, that is used in a Trust-Region Dogleg algorithm [25] to find up to six unique zeros of the right-hand side of Eq. (32), which correspond to the fixed points of interest. To assess the stability, the eigenvalues $\lambda_{1,2}$ of the Jacobian

$$J_{\Omega \approx 1} = \begin{bmatrix} -(\bar{\beta}_e + \bar{\beta}_m) + \frac{\bar{A}_x a}{8} \cos d - \frac{\bar{A}_y}{4} \sin d & -\left(\frac{\bar{A}_x a^2}{16} - \frac{\Omega^2 \bar{\theta}_{\max}}{2} - \frac{\bar{A}_x}{2}\right) \sin d - \frac{\bar{A}_y a}{2} \cos 2d \\ \frac{3a}{4} - \left(\frac{3\bar{A}_x}{16} - \frac{\Omega^2 \bar{\theta}_{\max}}{2a^2} - \frac{\bar{A}_x}{2a^2}\right) \sin d & -\left(\frac{3\bar{A}_x a}{16} - \frac{\Omega^2 \bar{\theta}_{\max}}{2a} - \frac{\bar{A}_x}{2a}\right) \cos d - \frac{\bar{A}_y}{2} \sin 2d \end{bmatrix}, \quad (35)$$

derived from Eq. (32) by treating the system as a vector-valued function with (a, d) as the input, are numerically evaluated at each fixed point, with stable fixed points satisfying $\text{Re}(\lambda_{1,2}) < 0$.

The amplitude of the free-oscillation term at steady state for the subharmonic response of Eq. (24) is found directly by solving Eq. (23), retaining only solutions satisfying $a \in \mathbb{R}$; d may then be found using Eq. (22) after averaging is

performed. For the subharmonic fixed points, the Jacobian

$$J_{\Omega \approx 3} = \begin{bmatrix} \bar{\beta}_e + \bar{\beta}_m & -\left(\sigma + 9\Lambda^2 - \frac{3\bar{A}_x\Lambda}{2}\right) \frac{a}{3} - \frac{3a^3}{8} \\ -\left(\sigma + 9\Lambda^2 - \frac{3\bar{A}_x\Lambda}{2}\right) \frac{1}{a} + \frac{9a}{8} & -3(\bar{\beta}_e + \bar{\beta}_m) \end{bmatrix},$$

derived from Eq. (22) after averaging is used to assess stability. To assess the stability of the $a = 0$ subharmonic solution, treat the solution amplitude a as flow on the line, since the dynamics of the phase d are irrelevant if the amplitude of the free-oscillation term is zero. Then

$$\frac{\partial a}{\partial T_1 \partial a} = -(\bar{\beta}_e + \bar{\beta}_m) + 2a \left(\frac{\bar{A}_x}{16} - \frac{3\Lambda}{4} \right) \cos d.$$

Hence,

$$\left. \frac{\partial a}{\partial T_1 \partial a} \right|_{a=0} = -(\bar{\beta}_e + \bar{\beta}_m),$$

which implies $a = 0$ is always stable for the subharmonic resonance.

Finally, the amplitude of the free-oscillation term at steady state for the superharmonic response of Eq. (27) is found directly by solving Eq. (26), again retaining only solutions satisfying $a \in \mathbb{R}$; d may then be found using Eq. (22) after averaging is performed. For the superharmonic fixed points, the Jacobian

$$J_{\Omega \approx \frac{1}{3}} = \begin{bmatrix} -(\bar{\beta}_e + \bar{\beta}_m) & -\left(\sigma + 3\Lambda^2 - \frac{\bar{A}_x\Lambda}{2}\right) a - \frac{3a^3}{8} \\ \left(\sigma + 3\Lambda^2 - \frac{\bar{A}_x\Lambda}{2}\right) \frac{1}{a} + \frac{9a}{8} & -(\bar{\beta}_e + \bar{\beta}_m) \end{bmatrix},$$

derived from averaged Eq. (22) is used to assess stability.

Figure 10 presents the amplitude of the numerical solution of Eq. (9), as well as the perturbation solutions to Eqs. (24), (27), and (33), versus frequency Ω for EX5. The correspondence is generally acceptable, especially considering that the forcing is not particularly weak. Notice the additional small resonance near $\Omega \approx 1/4$ that has not been resolved by the first-order expansion. The lack of numerical solution points that coincide with the

highest-amplitude branches in Fig. 10 should not be of concern, as the leftward bending of the superharmonic and primary resonances (sometimes referred to as the *foldover effect*) produces a hysteresis in the response, in which the path taken by the solution determines whether the steady-state response lies on the higher or lower solution branch. Since all numerical simulations begin with zero initial conditions, it is unsurprising that points tend not to lie on the uppermost branches. Some license has been

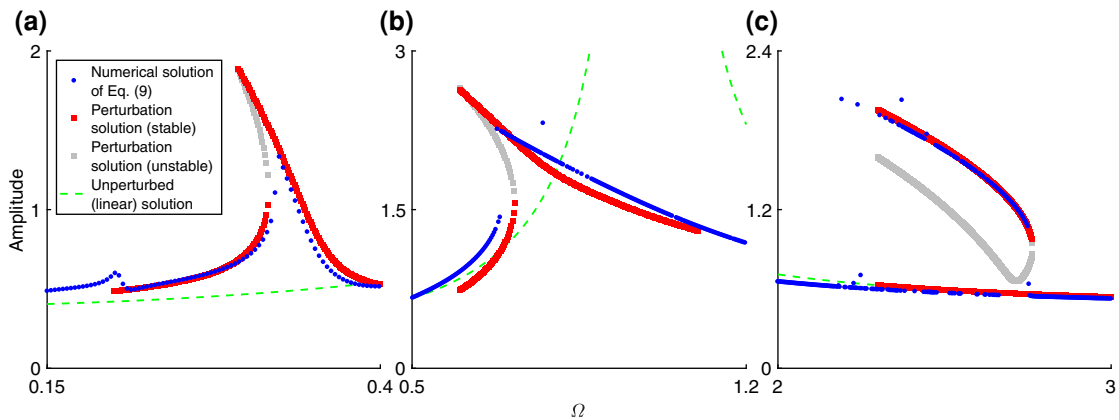


FIG. 10. Comparison of numerical and perturbation approximations of solution amplitude of (a) superharmonic resonance, (b) primary resonance, and (c) subharmonic resonance versus Ω for EX5.

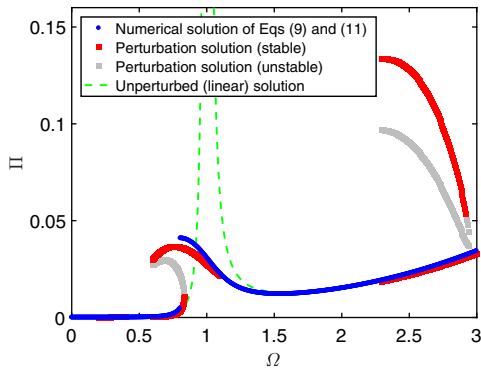


FIG. 11. Numerical versus analytical (linearization and perturbation) results for power versus frequency ratio using EX1 input.

taken in producing a comparison between numerical and approximate solutions, as the range of frequencies over which to plot the perturbation solution may be chosen freely, although solution accuracy degrades far from the solution’s corresponding resonance frequency.

Using the perturbation solutions to compute power, Fig. 7 may now be reproduced to help explain the nonlinear behavior under EX1, as shown in Fig. 11. Notice that the perturbation solutions predict the flat superharmonic response for EX1 and accurately predict the frequency of the onset of the primary resonance from the lower-amplitude solution branch. As the error in the approximate solutions propagates when power is computed using Eq. (11), the fit is not expected to be as close in a power versus frequency plot, such as Fig. 11.

An interesting feature of Fig. 11 is the existence of the high-amplitude subharmonic branch with no coinciding numerical solution points, which may seem concerning with respect to validation. However, much like the high-amplitude branches of the primary resonance, this can be explained by the fact that all numerical solutions of Eq. (9) are integrated using zero initial conditions in γ points that always lie outside of the small region of attraction for the high-amplitude branch of the subharmonic under EX1 in numerical simulations (Fig. 12).

Finally, Fig. 8 may be reproduced, again overlaying the power output of the perturbation solutions for EX5 (Fig. 13). The perturbation solutions again accurately capture the qualitative effect of the nonlinear resonance peaks and are fairly predictive of the frequency at which the lower solution branch of the primary resonance transitions to the higher-amplitude branch.

The perturbation solutions of the system approximation of Eq. (17) are therefore predictive of the dynamics of the true eccentric-rotor model of Eq. (9). The steady-state amplitudes of the perturbation solutions are in good agreement with the amplitudes of the numerical solutions of

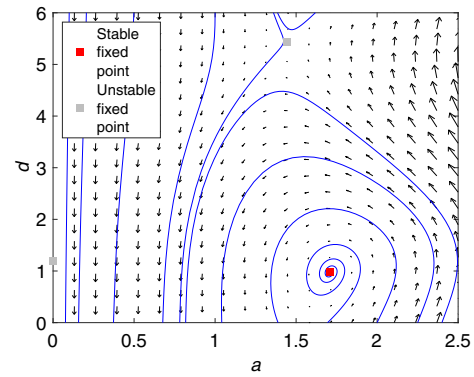


FIG. 12. Phase portrait of the a - d plane for the subharmonic resonance system, under EX1 at $\Omega = 2.5$. Region of attraction for the high-amplitude solution is small, and all simulated points corresponding to zero initial conditions approach $a = 0$ as $T_1 \rightarrow \infty$.

Eq. (9). Power output is more difficult to predict with accuracy, however, due to the propagation of error when the approximate solutions are used in Eq. (11), but qualitative effects of the solutions are captured well.

E. Invariance of power output at primary resonance

Compare the steady-state power output at the sharp transition to primary resonance for EX1 (Fig. 11) and EX5 (Fig. 13); remarkably, in spite of the substantial difference in the strength of the two excitations, the steady-state power output is nearly identical ($\Pi \approx 0.04$) in either case, possibly due to the effect of saturation. An interest in how the primary resonance peak behaves as the excitation is changed leads to the numerical investigation presented in Fig. 14, wherein the rotor model [Eq. (9)] is numerically integrated for Ω values near the primary resonance and power is again computed using Eq. (11). Recall that, for a given excitation, a change in Ω amounts to a change in the harvester’s natural frequency.

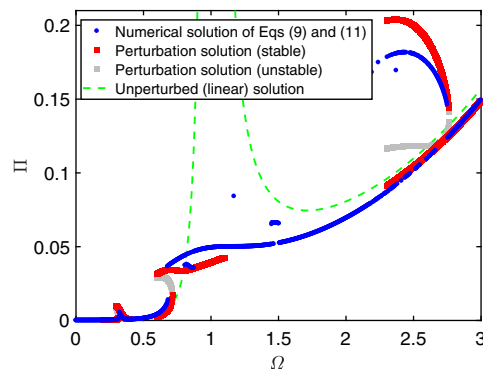


FIG. 13. Numerical versus analytical (linearization and perturbation) results for power versus frequency ratio using EX5 input.

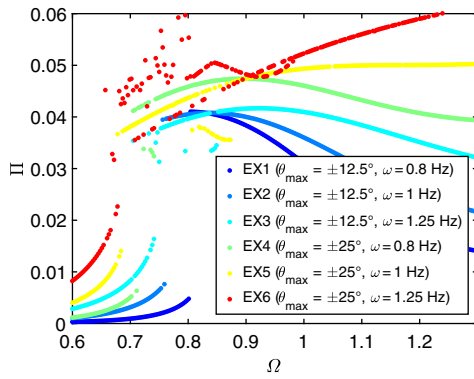


FIG. 14. Steady-state power output at primary resonance for all excitations from Table I.

The results of the numerical investigation of the primary resonance suggest that an eccentric rotor designed to exhibit a frequency ratio of $\Omega \approx 0.8$ under EX1 will continue to exhibit the high-amplitude response from swing arm excitation that the primary resonance affords, even with increasing input frequency (as this shifts Ω rightward) and swing arm amplitude.

F. Summary

Some of the primary results of the analysis presented in this section are succinctly listed below:

(a) The eccentric-rotor model [Eq. (9)] exhibits behavior characteristic of a Duffing oscillator with a softening spring nonlinearity, in spite of differences in nonlinearities and the addition of parametric excitation. This includes secondary resonances at $\Omega \approx 1/3$ and $\Omega \approx 3$ and a primary resonance exhibiting the foldover effect.

(b) The peak at $\Omega \approx 1/3$ is a nonlinear superharmonic resonance. Its magnitude relative to the primary resonance is generally small and is strongly dependent on the forcing.

(c) The peak at $\Omega \approx 3$ is a nonlinear subharmonic resonance. Its magnitude is large and it extends over a wide range of Ω values; however, the coexistence of high-amplitude and low-amplitude solution branches and seemingly small regions of attraction for the high-amplitude branch under weak forcing suggest that consistent operation at the high-amplitude branch would be difficult to achieve in practice.

(d) The amplitude of the primary resonance is highly consistent under all excitations listed in Table I, and the behavior of this peak provides an exploitable design opportunity.

V. RESONANT ECCENTRIC-ROTOR DESIGN

Following observations of the behavior of the primary resonance peak in Sec. IV, a resonant eccentric-rotor

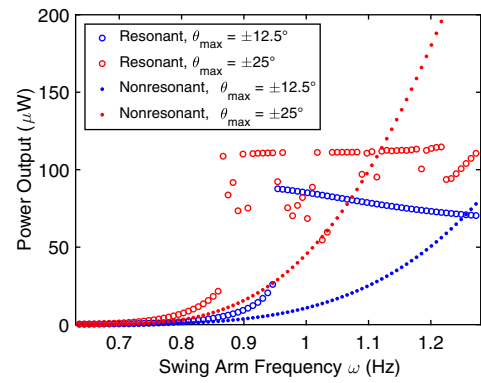


FIG. 15. Power versus swing arm frequency for two example resonant and nonresonant eccentric-rotor designs.

harvester design is proposed and evaluated against a comparable nonresonant design.

Consider again, as in Sec. III, a homogeneous tungsten cylindrical sector rotor geometry with density $\rho = 19000 \text{ kg m}^{-3}$, angle α , radius r , height h , total device volume $\pi r^2 h = 1 \text{ cm}^3$, and thickness 2 mm, requiring a radius $r \approx 12.6 \text{ mm}$. By prudent selection of the effective length, l_{eff} , an eccentric-rotor design with a frequency ratio $\Omega \approx 0.8$ under EX1 may be obtained; an effective length of $l_{\text{eff}} \approx 0.18 \text{ m}$ is one such choice, which can be realized with an angle $\alpha \approx 5.97 \text{ rad}$, which is nearly a full cylinder of tungsten. Whether such a resonant design will maintain a high power output as the forcing parameters A_x and A_y change with the input frequency can be ascertained via numerical simulation of the dimensioned system [Eq. (3)]. A choice of $b_e = 1.3 \times 10^{-6} \text{ N m s rad}^{-1}$ for the electrical damping coefficient is selected for the resonant device. The optimized nonresonant device from Sec. III ($\alpha \approx 3.44 \text{ rad}$, $b_e = 8.6 \times 10^{-6} \text{ N m s rad}^{-1}$) is selected as a benchmark against which to gauge the performance of the resonant device. Equation (3) is solved numerically for each device over a period for 20 swing arm cycles, and the final three swing arm periods are used as the time span t_0 in Eq. (4) over which power output is calculated. A mechanical damping coefficient of $b_m = 8.6 \times 10^{-6} \text{ N m s rad}^{-1}$ is used to represent loss in each device. The results of the numerical simulations are presented in Fig. 15.

As observed in Fig. 15, the resonant design is capable of producing a high power output over a large range of swing arm frequencies. Only at the highest frequencies simulated does the nonresonant design begin to outperform the resonant design. However, the nonresonant design benefits tremendously from the high degree of electrical damping, which is nearly 7 times as high as the electrical damping of the resonant device. To realize such a level of damping in practice, some additional portion of the device volume would need to be consumed by a transducer, which is volume that could otherwise be utilized

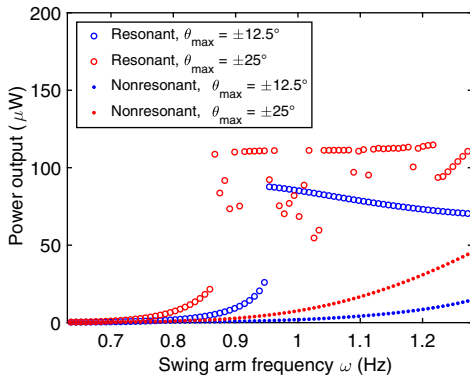


FIG. 16. Power versus swing arm frequency for two example resonant and nonresonant eccentric-rotor designs with equal values of electrical damping.

by additional harvester mass. For a more fair comparison, another set of simulations using an electrical damping coefficient of $b_e = 1.3 \times 10^{-6} \text{ N m s rad}^{-1}$ for *both* devices is performed (Fig. 16).

As evidenced in Fig. 16, a resonant design is capable of producing higher power over a wider range of swing arm frequencies than that of a comparable nonresonant device, when the device volumes and electrical damping coefficients are matched.

It is also worth noting that the design of a rotor with a wideband response at the primary resonance peak is aided by a mild self-tuning phenomenon of the eccentric rotor over the range of excitations considered in Table I. Recall that the natural frequency $\omega_0 = \sqrt{\bar{y}/I_{\text{eff}}}$, and that the average y acceleration $\bar{y} = g(1 - \theta_{\text{max}}^2/4) + \theta_{\text{max}}^2 I_{\text{arm}} \omega^2/2$. This means that $\omega_0 = \omega_0(\omega)$, which increases as the input excitation frequency ω increases — that is, the harvester resonance frequency tends to move with the input frequency. This effect is observed and exploited in other energy-harvesting devices with pendulum dynamics [26, 27].

VI. CONCLUSIONS

The dynamical analysis of an eccentric-rotor harvester under swing arm excitation is presented. A linearized system model predicts the behavior of nonresonant devices well, if the natural frequency of the device is far from the primary resonance or nonlinear secondary resonances. It is shown that the eccentric-rotor harvester behaves very similarly to a Duffing oscillator with softening spring nonlinearity. The relatively small magnitude of the superharmonic resonance, and the coexistence of high- and low-amplitude solution branches for the subharmonic resonance, makes targeting these resonance peaks in a practical design challenging. However, the behavior of the primary resonance peak makes it ideal for harvesting, since power output appears insensitive to changes in input excitations at

this resonance. A resonant eccentric harvester is proposed to exploit this behavior and its performance compared to a nonresonant design via simulation to demonstrate its consistently high power output.

The entire analysis presented here assumes a steady-state harvesting condition; for excitations derived from human motion, this is likely to be a rare operating condition. Future work should incorporate transient analysis, as this may have a significant impact on the design approach for an eccentric-rotor harvester. Additionally, analysis of the model subject to stochastic input vibrations could provide useful design insight, considering the input excitation in practical applications is perhaps better characterized by statistical properties than by deterministic harmonic functions.

ACKNOWLEDGMENTS

The authors would like to express their gratitude to Alexander Balk and Andrejs Treibergs for their generosity with their time spent participating in discussions on perturbation methods and nondimensionalization, as well as Analog Devices Inc., for the grant that made this work possible.

APPENDIX

Derivation of the approximate analytical solutions presented in Sec. IV requires considerable mathematical manipulation that has been largely omitted for brevity. This appendix contains an augmented derivation of the primary results of Sec. IV, presented in tutorial fashion, for the convenience of the reader.

To apply the method of averaging to the secondary resonances, the method of variation of parameters is first applied. The solution of Eq. (18) with $\epsilon = 0$ is

$$\gamma = a \cos(\tau + b) + 2\Lambda \sin \Omega \tau, \quad (\text{A1})$$

where the *free-oscillation* term is $a \cos(\tau + b)$ with a and b as variables, which are sometimes referred to as *parameters*, and $\Lambda = (A_x + \Omega^2 \theta_{\text{max}})/[2(1 - \Omega^2)]$. Notably, Eq. (A1) contains a term with a small divisor, Λ , that becomes large as $\Omega \rightarrow 1$; the existence of this term is why the primary and secondary resonances are treated separately in this analysis.

When $\epsilon \neq 0$, it is assumed that the solution is still given by Eq. (A1), but with slowly time-varying parameters $a(T_1)$ and $b(T_1)$. The solution to Eq. (A1) may be viewed as a transformation from $\gamma(\tau)$ to $a(T_1)$ and $b(T_1)$. As a consequence, there is freedom in choosing an additional equation that imposes a condition on the unknown functions. A convenient choice is taking the (dimensionless) time derivative of Eq. (A1), while treating a and b as

constants:

$$\gamma' = -a \sin(\tau + b) + 2\Lambda\Omega \cos \Omega\tau. \quad (\text{A2})$$

However, when $\epsilon \neq 0$, the solution is still of the form of Eq. (A1), subject to the constraint of Eq. (A2), but with $a = a(\tau)$ and $b = b(\tau)$. Differentiation of Eq. (A1) in light of this gives

$$\begin{aligned} \gamma' &= -a \sin(\tau + b) + a' \cos(\tau + b) - ab' \sin(\tau + b) \\ &\quad + 2\Lambda\Omega \cos \Omega\tau. \end{aligned} \quad (\text{A3})$$

Equation (A2) with Eq. (A3) implies

$$a' \cos(\tau + b) - ab' \sin(\tau + b) = 0. \quad (\text{A4})$$

Differentiating Eq. (A2) once more yields

$$\begin{aligned} \gamma'' &= -a \cos(\tau + b) - a' \sin(\tau + b) - ab' \cos(\tau + b) \\ &\quad - 2\Lambda\Omega^2 \sin \Omega\tau. \end{aligned} \quad (\text{A5})$$

Substitution of Eqs. (A1), (A2), and (A5) into Eq. (18) gives

$$\begin{aligned} &-a \cos(\tau + b) - a' \sin(\tau + b) \\ &-ab' \cos(\tau + b) - 2\Lambda\Omega^2 \sin \Omega\tau \\ &+a \cos(\tau + b) + 2\Lambda \sin \Omega\tau \\ &+ \epsilon \left\{ \begin{aligned} &2(\bar{\beta}_e + \bar{\beta}_m)[-a \sin(\tau + b) + 2\Lambda\Omega \cos \Omega\tau] \\ &+\bar{A}_y \cos 2\Omega\tau[a \cos(\tau + b) + 2\Lambda \sin \Omega\tau] \\ &+\frac{1}{2}\bar{A}_x \sin \Omega\tau[a \cos(\tau + b) + 2\Lambda \sin \Omega\tau]^2 \\ &-[a \cos(\tau + b) + 2\Lambda \sin \Omega\tau]^3 - \bar{A}_x \sin \Omega\tau \end{aligned} \right\} \\ &= \Omega^2 \theta_{\max} \sin \Omega\tau. \end{aligned} \quad (\text{A6})$$

where interest in a first-order expansion allows for the dropping of $O(\epsilon^2)$; this is made more plain from substitution of Eq. (20) into Eq. (18) with retention of terms up to $O(\epsilon)$, although such a procedure requires more algebra. As $\Lambda = (A_x + \Omega^2 \theta_{\max})/[2(1 - \Omega^2)]$, Eq. (A6) reduces to

$$\begin{aligned} &a' \sin(\tau + b) + ab' \cos(\tau + b) \\ &= \epsilon \left\{ \begin{aligned} &2(\bar{\beta}_e + \bar{\beta}_m)[-a \sin(\tau + b) + 2\Lambda\Omega \cos \Omega\tau] \\ &+\bar{A}_y \cos 2\Omega\tau[a \cos(\tau + b) + 2\Lambda \sin \Omega\tau] \\ &+\frac{1}{2}\bar{A}_x \sin \Omega\tau[a \cos(\tau + b) + 2\Lambda \sin \Omega\tau]^2 \\ &-[a \cos(\tau + b) + 2\Lambda \sin \Omega\tau]^3 - \bar{A}_x \sin \Omega\tau \end{aligned} \right\}. \end{aligned} \quad (\text{A7})$$

Multiply Eq. (A4) by $\cos(\tau + b)$ and Eq. (A7) by $\sin(\tau + b)$ and add the result to obtain

$$\begin{aligned} a' &= \epsilon \sin(\tau + b) \\ &\left\{ \begin{aligned} &2(\bar{\beta}_e + \bar{\beta}_m)[-a \sin(\tau + b) + 2\Lambda\Omega \cos \Omega\tau] \\ &+\bar{A}_y \cos 2\Omega\tau[a \cos(\tau + b) + 2\Lambda \sin \Omega\tau] \\ &+\frac{1}{2}\bar{A}_x \sin \Omega\tau[a \cos(\tau + b) + 2\Lambda \sin \Omega\tau]^2 \\ &-[a \cos(\tau + b) + 2\Lambda \sin \Omega\tau]^3 - \bar{A}_x \sin \Omega\tau \end{aligned} \right\}. \end{aligned} \quad (\text{A8})$$

which defines the dynamics of the parameter a . The differential equation for b may be obtained similarly by multiplying Eq. (A4) by $\sin(\tau + b)$ and Eq. (A7) by $\cos(\tau + b)$ and adding the result to obtain

$$\begin{aligned} ab' &= \epsilon \cos(\tau + b) \\ &\left\{ \begin{aligned} &2(\bar{\beta}_e + \bar{\beta}_m)[-a \sin(\tau + b) + 2\Lambda\Omega \cos \Omega\tau] \\ &+\bar{A}_y \cos 2\Omega\tau[a \cos(\tau + b) + 2\Lambda \sin \Omega\tau] \\ &+\frac{1}{2}\bar{A}_x \sin \Omega\tau[a \cos(\tau + b) + 2\Lambda \sin \Omega\tau]^2 \\ &-[a \cos(\tau + b) + 2\Lambda \sin \Omega\tau]^3 - \bar{A}_x \sin \Omega\tau \end{aligned} \right\}. \end{aligned} \quad (\text{A9})$$

Expanding Eqs. (A8) and (A9) and grouping by the argument of the trigonometric functions gives

$$\begin{aligned} \frac{\partial a}{\partial T_1} &= -(\bar{\beta}_e + \bar{\beta}_m)a \\ &+ \left(\frac{\bar{A}_x a^2}{16} - \frac{3\Lambda a^2}{4} \right) \cos[(3 - \Omega)\tau + 3b] \\ &+ \left(\Lambda^3 - \frac{\bar{A}_x \Lambda^2}{4} + \frac{\bar{A}_y \Lambda}{2} \right) \cos[(1 - 3\Omega)\tau + b] \\ &+ \text{OT}, \\ a \frac{\partial b}{\partial T_1} &= -3\Lambda^2 a + \frac{\bar{A}_x \Lambda a}{2} - \frac{3a^3}{8} \\ &+ \left(-\frac{\bar{A}_x a^2}{16} + \frac{3\Lambda a^2}{4} \right) \sin[(3 - \Omega)\tau + 3b] \\ &+ \left(-\Lambda^3 + \frac{\bar{A}_x \Lambda^2}{4} - \frac{\bar{A}_y \Lambda}{2} \right) \sin[(1 - 3\Omega)\tau + b] \\ &+ \left(3\Lambda^2 a - \frac{\bar{A}_x \Lambda a}{2} + \frac{\bar{A}_y a}{2} \right) \cos 2\Omega\tau + \text{OT}, \end{aligned} \quad (\text{A10})$$

where the substitution $\partial/\partial T_0 = \epsilon \partial/\partial T_1$ allows for elimination of ϵ and OT refers to other terms that are immaterial with regard to the method of averaging near the secondary resonances, such as $\sin[(1 + 3\Omega)\tau + b]$ or

$\cos[(3 + \Omega)\tau + b]$, as these rapidly varying terms average to zero for the secondary resonances near $\Omega \approx 3$ and $\Omega \approx 1/3$. Special consideration is required at $\Omega \approx 0$.

The terms in Eq. (A10) are examined to demarcate frequencies of interest for the analysis.

For the case of $\Omega \approx 3$, the slowly varying trigonometric terms in Eq. (A10) are $\cos[(3 - \Omega)\tau + 3b]$ and $\sin[(3 - \Omega)\tau + 3b]$; retention of only slowly varying terms represents a simple procedure for averaging the vector field. Thus, the solution parameters are governed by

$$\begin{aligned}\frac{\partial a}{\partial T_1} &= -(\bar{\beta}_e + \bar{\beta}_m)a + \left(\frac{\bar{A}_x a^2}{16} - \frac{3\Lambda a^2}{4}\right) \cos[(3 - \Omega)\tau + 3b], \\ a \frac{\partial b}{\partial T_1} &= -3\Lambda^2 a + \frac{\bar{A}_x \Lambda a}{2} - \frac{3a^3}{8} + \left(-\frac{\bar{A}_x a^2}{16} + \frac{3\Lambda a^2}{4}\right) \sin[(3 - \Omega)\tau + 3b].\end{aligned}\quad (\text{A11})$$

Substitute $\Omega = 3 + \epsilon\sigma$, where σ is referred to as a *detuning parameter* that is used to express the propinquity of Ω to three, into Eq. (A11) to give

$$\begin{aligned}\frac{\partial a}{\partial T_1} &= -(\bar{\beta}_e + \bar{\beta}_m)a + \left(\frac{\bar{A}_x a^2}{16} - \frac{3\Lambda a^2}{4}\right) \cos[T_1\sigma - 3b], \\ a \frac{\partial b}{\partial T_1} &= -3\Lambda^2 a + \frac{\bar{A}_x \Lambda a}{2} - \frac{3a^3}{8} + \left(\frac{\bar{A}_x a^2}{16} - \frac{3\Lambda a^2}{4}\right) \sin[T_1\sigma - 3b].\end{aligned}\quad (\text{A12})$$

To make Eq. (A12) autonomous, introduce a new independent variable

$$d = T_1\sigma - 3b. \quad (\text{A13})$$

Hence,

$$\frac{\partial d}{\partial T_1} = \sigma - 3 \frac{\partial b}{\partial T_1}. \quad (\text{A14})$$

Substituting Eqs. (A13) and (A14) into Eq. (A12) and simplifying yields

$$\begin{aligned}\frac{\partial a}{\partial T_1} &= -(\bar{\beta}_e + \bar{\beta}_m)a + a^2 \left(\frac{\bar{A}_x}{16} - \frac{3\Lambda}{4}\right) \cos d, \\ a \frac{\partial d}{\partial T_1} &= \sigma a + 9\Lambda^2 a - \frac{3\bar{A}_x \Lambda a}{2} + \frac{9a^3}{8} \\ &\quad - 3a^2 \left(\frac{\bar{A}_x}{16} - \frac{3\Lambda}{4}\right) \sin d,\end{aligned}\quad (\text{A15})$$

which are now autonomous. It may appear that not much progress has been made; the nonlinear system in Eq. (17) has been replaced by another nonlinear system, Eq. (A15). However, the parameters in Eq. (A15) approach stationary values with increasing T_1 , in which case the free-oscillation term in Eq. (A1) achieves a periodic steady state

with fixed amplitude. Letting $\partial a/\partial T_1 = \partial d/\partial T_1 = 0$ then, with some manipulation, d may be eliminated entirely, leaving

$$\begin{aligned}81a^4 + 64 \left[\frac{81\Lambda^2}{4} - \frac{27\bar{A}_x \Lambda}{8} + \frac{9\sigma}{4} - \frac{5}{2}(\bar{A}_x - 12\Lambda)^2 \right] a^2 \\ + 16(18\Lambda^2 - 3\bar{A}_x \Lambda + 2\sigma)^2 + 64(\bar{\beta}_e + \bar{\beta}_e)^2 = 0,\end{aligned}\quad (\text{A16})$$

which is quadratic in a^2 and easily solved. Equation (A16) is often referred to as a *frequency response equation*, and it relates the amplitude of the free-oscillation term to the frequency σ . For solutions satisfying $a^2 \in \mathbb{R}$, the discriminant of the solution satisfying Eq. (A16) must be positive.

Equation (A16) is derived by neglecting the $a = 0$ solution, which is a solution of particular interest, since this implies that the free-oscillation term in Eq. (21) vanishes.

The vector field that governs the subharmonic solution parameters, Eq. (A15), under EX1 is visualized in Fig. 12.

Substitution of $b = T_1\sigma/3 - d/3$ from Eq. (A13), along with $\Omega = 3 + \epsilon\sigma$ and $T_1 = \epsilon\tau$, into Eq. (20) gives the solution

$$y = a \cos\left(\frac{1}{3}\Omega\tau - \frac{1}{3}d\right) + 2\Lambda \sin \Omega\tau + O(\epsilon),$$

up to $O(\epsilon)$ with (dimensionless) time derivative

$$\gamma' = -\frac{1}{3}a\Omega \sin\left(\frac{1}{3}\Omega\tau - \frac{1}{3}d\right) + 2\Lambda\Omega \cos\Omega\tau + O(\epsilon),$$

for the case of $\Omega \approx 3$.

For the case of $\Omega \approx 1/3$, the slowly varying trigonometric terms in Eq. (A10) are $\cos[(1 - 3\Omega)\tau + b]$ and $\sin[(1 - 3\Omega)\tau + b]$. Thus, the parameters are governed by

$$\begin{aligned} \frac{\partial a}{\partial T_1} &= -(\bar{\beta}_e + \bar{\beta}_m)a + \left(\Lambda^3 - \frac{\bar{A}_x\Lambda^2}{4} + \frac{\bar{A}_y\Lambda}{2}\right) \cos[(1 - 3\Omega)\tau + b], \\ a\frac{\partial b}{\partial T_1} &= -3\Lambda^2a + \frac{\bar{A}_x\Lambda a}{2} - \frac{3a^3}{8} + \left(-\Lambda^3 + \frac{\bar{A}_x\Lambda^2}{4} - \frac{\bar{A}_y\Lambda}{2}\right) \sin[(1 - 3\Omega)\tau + b]. \end{aligned} \quad (\text{A17})$$

Similar to the case of $\Omega \approx 3$, a detuning parameter σ is introduced, satisfying $3\Omega = 1 + \epsilon\sigma$, as well as a new independent parameter defined by $d = \sigma T_1 - b$, so that Eq. (A17) may be rewritten as an autonomous system in a and d :

$$\begin{aligned} \frac{\partial a}{\partial T_1} &= -(\bar{\beta}_e + \bar{\beta}_m)a + \left(\Lambda^3 - \frac{\bar{A}_x\Lambda^2}{4} + \frac{\bar{A}_y\Lambda}{2}\right) \cos d, \\ a\frac{\partial d}{\partial T_1} &= \sigma a + 3\Lambda^2a - \frac{\bar{A}_x\Lambda a}{2} + \frac{3a^3}{8} - \left(\Lambda^3 - \frac{\bar{A}_x\Lambda^2}{4} + \frac{\bar{A}_y\Lambda}{2}\right) \sin d. \end{aligned} \quad (\text{A18})$$

Finding the fixed points of Eq. (A18) with subsequent elimination of d yields

$$\begin{aligned} \frac{9}{64}a^6 + \left(\frac{9\Lambda^2}{4} - \frac{3\bar{A}_x\Lambda}{8} + \frac{3\sigma}{4}\right)a^4 + \left[\left(3\Lambda^2 - \frac{\bar{A}_x\Lambda}{2} + \sigma\right)^2 + (\bar{\beta}_e + \bar{\beta}_m)^2\right]a^2 \\ - 2\left(\Lambda^3 - \frac{\bar{A}_x\Lambda^2}{4} + \frac{\bar{A}_y\Lambda}{2}\right)^2 = 0, \end{aligned} \quad (\text{A19})$$

which is a cubic equation in a^2 . The roots of Eq. (A19) satisfying $a^2 \in \mathbb{R}$ give the steady-state amplitude of the free-oscillation for a given σ .

Since $b = \sigma T_1 - d$, $3\Omega = 1 + \epsilon\sigma$, and $T_1 = \epsilon\tau$, the solution for the case of $\Omega \approx 1/3$ is given by

$$\gamma = a \cos(3\Omega\tau - d) + 2\Lambda \sin\Omega\tau + O(\epsilon),$$

up to $O(\epsilon)$ with time derivative

$$\gamma' = -3a\Omega \sin(3\Omega\tau - d) + 2\Lambda\Omega \cos\Omega\tau + O(\epsilon).$$

The analysis of the primary resonance proceeds as with that of the secondary resonances. The solution of Eq. (30) with $\epsilon = 0$ is

$$\gamma = a \cos(\tau + b), \quad (\text{A20})$$

where a and b again act as solution parameters. Notice that Eq. (A20) no longer contains the small divisor term. Taking the (dimensionless) time derivative of Eq. (A20), while treating a and b as constants gives

$$\gamma' = -a \sin(\tau + b). \quad (\text{A21})$$

However, when $\epsilon \neq 0$, the solution is still of the form Eq. (A20), subject to the constraint of Eq. (A21), but with $a = a(\tau)$ and $b = b(\tau)$. Differentiation of Eq. (A20) in light of this gives

$$\gamma' = -a \sin(\tau + b) + a' \cos(\tau + b) - ab' \sin(\tau + b). \quad (\text{A22})$$

Equation (A21) with Eq. (A22) implies

$$a' \cos(\tau + b) - ab' \sin(\tau + b) = 0. \quad (\text{A23})$$

Differentiating Eq. (A21) once more yields

$$\gamma'' = -a \cos(\tau + b) - a' \sin(\tau + b) - ab' \cos(\tau + b). \quad (\text{A24})$$

Substitution of Eqs. (A20), (A21), and (A24) into Eq. (30) with some simplification gives

$$a' \sin(\tau + b) + ab' \cos(\tau + b) = \epsilon \begin{bmatrix} -2a(\bar{\beta}_e + \bar{\beta}_m) \sin(\tau + b) \\ + a\bar{A}_y \cos 2\Omega\tau \cos(\tau + b) \\ + \frac{1}{2}a^2\bar{A}_x \sin \Omega\tau \cos^2(\tau + b) \\ - a^3 \cos^3(\tau + b) - (\Omega^2\bar{\theta}_{\max} + \bar{A}_x) \sin \Omega\tau \end{bmatrix}, \quad (\text{A25})$$

where the $O(\epsilon^2)$ term is again ignored. As with the secondary resonances, Eq. (A25) is used along with Eq. (A23) to solve for a'

$$a' = \epsilon \sin(\tau + b) \begin{bmatrix} -2a(\bar{\beta}_e + \bar{\beta}_m) \sin(\tau + b) + a\bar{A}_y \cos 2\Omega\tau \cos(\tau + b) \\ + \frac{1}{2}a^2\bar{A}_x \sin \Omega\tau \cos^2(\tau + b) - a^3 \cos^3(\tau + b) \\ - (\Omega^2\bar{\theta}_{\max} + \bar{A}_x) \sin \Omega\tau \end{bmatrix}, \quad (\text{A26})$$

and ab'

$$ab' = \epsilon \cos(\tau + b) \begin{bmatrix} -2a(\bar{\beta}_e + \bar{\beta}_m) \sin(\tau + b) \\ + a\bar{A}_y \cos 2\Omega\tau \cos(\tau + b) \\ + \frac{1}{2}a^2\bar{A}_x \sin \Omega\tau \cos^2(\tau + b) \\ - a^3 \cos^3(\tau + b) - (\Omega^2\bar{\theta}_{\max} + \bar{A}_x) \sin \Omega\tau \end{bmatrix}. \quad (\text{A27})$$

Expanding Eqs. (A26) and (A27), eliminating ϵ , and noting that the slowly varying trigonometric terms are $\cos[(1 - \Omega)\tau + b]$ and $\sin[(1 - \Omega)\tau + b]$, as well as $\sin[2(1 - \Omega)\tau + 2b]$ and $\cos[2(1 - \Omega)\tau + 2b]$, gives

$$\begin{aligned} \frac{\partial a}{\partial T_1} &= -(\bar{\beta}_e + \bar{\beta}_m)a + \left(\frac{\bar{A}_x a^2}{16} - \frac{\Omega^2 \bar{\theta}_{\max}}{2} - \frac{\bar{A}_x}{2} \right) \cos[(1 - \Omega)\tau + b] + \frac{\bar{A}_y a}{4} \sin[2(1 - \Omega)\tau + 2b], \\ a \frac{\partial b}{\partial T_1} &= -\frac{3a^3}{8} + \left(-\frac{3\bar{A}_x a^2}{16} + \frac{\Omega^2 \bar{\theta}_{\max}}{2} + \frac{\bar{A}_x}{2} \right) \sin[(1 - \Omega)\tau + b] + \frac{\bar{A}_y a}{4} \cos[2(1 - \Omega)\tau + 2b]. \end{aligned} \quad (\text{A28})$$

Finally, the detuning parameter σ is introduced, defined by $\Omega = 1 + \epsilon\sigma$, as well as a new independent parameter satisfying $d = \sigma T_1 - b$, so that Eq. (A28) can be represented by the autonomous system

$$\begin{aligned} \frac{\partial a}{\partial T_1} &= -(\bar{\beta}_e + \bar{\beta}_m)a + \left(\frac{\bar{A}_x a^2}{16} - \frac{\Omega^2 \bar{\theta}_{\max}}{2} - \frac{\bar{A}_x}{2} \right) \cos d - \frac{\bar{A}_y a}{4} \sin 2d, \\ a \frac{\partial d}{\partial T_1} &= a\sigma + \frac{3a^3}{8} + \left(-\frac{3\bar{A}_x a^2}{16} + \frac{\Omega^2 \bar{\theta}_{\max}}{2} + \frac{\bar{A}_x}{2} \right) \sin d - \frac{\bar{A}_y a}{4} \cos 2d. \end{aligned} \quad (\text{A29})$$

- [1] P. Pillatsch, E. M. Yeatman, and A. S. Holmes, A piezoelectric frequency up-converting energy harvester with rotating proof mass for human body applications, *Sens. Actuators, A Phys.* **206**, 178 (2014).
- [2] L. Xie and R. Du, Harvest human kinetic energy to power portable electronics, *J. Mech. Sci. Technol.* **26**, 2005 (2012).
- [3] T. Xue, X. Ma, C. Rahn, and S. J. Roundy, in *J. Phys. Conf. Ser.* (2014).
- [4] R. Lockhart, P. Janphuang, D. Briand, and N. F. de Rooij, in *2014 IEEE 27th Int. Conf. Micro Electro Mech. Syst.* (2014), pp. 370–373.
- [5] E. Romero, M. R. Neuman, and R. O. Warrington, in *2011 IEEE 24th Int. Conf. Micro Electro Mech. Syst.* (2011), pp. 1325–1328.
- [6] J. Nakano, K. Komori, Y. Hattori, and Y. Suzuki, in *J. Phys. Conf. Ser.* (2015).
- [7] M. Adachi, T. Miyoshi, K. Suzuki, Q. Fu, Q. Fang, and Y. Suzuki, in *J. Phys. Conf. Ser.* (2018).
- [8] M. Hayakawa, US5001685 A (1991).
- [9] Kinetron, *Micro Generator System “26.4”* (2014).
- [10] F. J. Romeiras and E. Ott, Strange Nonchaotic Attractors of the Damped Pendulum with Quasiperiodic Forcing, *Phys. Rev. Appl.* **35**, 4404 (1987).
- [11] J. B. McLaughlin, Period-doubling bifurcations and chaotic motion for a parametrically forced pendulum, *J. Stat. Phys.* **24**, 375 (1981).
- [12] B. P. Koch and R. W. Leven, Subharmonic and homoclinic bifurcations in a parametrically forced pendulum, *Phys. D: Nonlinear Phenom.* **16**, 1 (1985).
- [13] X. Xu and M. Wiercigroch, Approximate analytical solutions for oscillatory and rotational motion of a parametric pendulum, *Nonlinear Dyn.* **47**, 311 (2007).
- [14] R. Rantz, M. A. Halim, T. Xue, Q. Zhang, L. Gu, K. Yang, and S. Roundy, Architectures for wrist-worn energy harvesting, *Smart Mater. Struct.* **27**, 044001 (2018).
- [15] A. Cadei, A. Dionisi, E. Sardini, and M. Serpelloni, Kinetic and thermal energy harvesters for implantable medical devices and biomedical autonomous sensors, *Meas. Sci. Technol.* **25**, 012003 (2014).
- [16] E. Romero, R. O. Warrington, M. R. Neuman, and S. Member, in *2009 Annu. Int. Conf. IEEE Eng. Med. Biol. Soc.* (2009), pp. 2752–2755.
- [17] B. Gutnik, H. MacKie, G. Hudson, and C. Standen, How close to a pendulum is human upper limb movement during walking?, *HOMO- J. Comp. Hum. Biol.* **56**, 35 (2005).
- [18] D. Webb, R. H. Tuttle, and M. Baksh, Pendular activity of human upper limbs during slow and normal walking, *Am. J. Phys. Anthropol.* **93**, 477 (1994).
- [19] P. D. Mitcheson, T. C. Green, E. M. Yeatman, and A. S. Holmes, Architectures for vibration-driven micropower generators, *J. Microelectromech. Syst.* **13**, 429 (2004).
- [20] C. B. Williams and R. B. Yates, Analysis of a micro-electric generator for microsystems, *Sens. Actuators, A Phys.* **52**, 8 (1996).
- [21] S. J. Roundy, P. K. Wright, and J. Rabaey, A study of low level vibrations as a power source for wireless sensor nodes, *Comput. Commun.* **26**, 1131 (2003).
- [22] S. J. Roundy and P. K. Wright, A piezoelectric vibration based generator for wireless electronics, *Smart Mater. Struct.* **13**, 1131 (2004).
- [23] D. W. Jordan and P. Smith, *Nonlinear Ordinary Differential Equations: An Introduction for Scientists and Engineers*, 4th ed (Oxford University Press, Oxford, England, 2007).
- [24] N. Hasan, *Introduction to Perturbation Techniques* (John Wiley & Sons, Inc., New York, 1993).
- [25] M. J. D. Powell, *Numerical Methods for Nonlinear Algebraic Equations*, P. Rabinow (1970).
- [26] L. Gu, C. Livermore, and U. States, in *Power MEMS Work. Leuven, Belgium* (2010).
- [27] S. Roundy and J. Tola, Energy harvester for rotating environments using offset pendulum and nonlinear dynamics, *Smart Mater. Struct.* **23**, 105004 (2014).